Journal of Materials Chemistry A

PAPER

Nitrogen-doped carbon and iron carbide nanocomposites as cost-effective counter electrodes of dye-sensitized solar cells†

Cite this: J. Mater. Chem. A, 2014, 2, 4676

Hongxia Xu,‡[a] Chuanjian Zhang,‡[a] Zaiwei Wang,[ab] Shuping Pang,[a] Xinhong Zhou,*[c] Zhongyi Zhang[a] and Guanglei Cui*[a]

Received 30th October 2013
Accepted 3rd January 2014

DOI: 10.1039/c3ta14429a

www.rsc.org/MaterialsA

Hierarchical nanocomposites of iron carbide (Fe_3C) encaged in nitrogen-doped carbon (N–C) were prepared by using a simple carbothermal reduction of iron(II) oxalate (FeC_2O_4) nanowires in the presence of cyanamide (NH_2CN) at 600 °C. Such Fe_3C@N–C nanocomposites delivered fair electrocatalytic activity for the I_3^-/I^- redox reaction. As a result, when explored as cost-effective counter electrodes of dye-sensitized solar cells, an efficiency of 7.36% was achieved, which was comparable to that of the cell with a Pt–FTO counter electrode (7.15%) under the same experimental conditions. The good electrochemical performance is attributed to the synergistic effect of the combination of N–C and Fe_3C and the one dimensional configuration, which endows the nanocomposites with more interfacial active sites and improved electron transfer efficiency for the reduction of I_3^-/I^-.

Introduction

Nanocrystalline dye-sensitized solar cells (DSSCs), introduced by Grätzel and O'Regan in 1991, have attracted considerable attention from academic and industrial fields because of their cost effectiveness and comparable high light-to-electricity conversion efficiency (η), and their ease of manufacturing.[1–6] The counter electrodes (CE), as one of essential components of the DSSCs, are usually composed of the noble metal platinum (Pt) coated on transparent conductive oxides (such as indium-doped tin oxide). However, the limited supply and the high cost of Pt hinders its large-scale commercial applications in DSSCs counter electrodes.[7,8] Therefore, it is imperative to develop low-cost, abundant and highly-efficient substitutes for the conventional Pt counter electrode in the DSSC system. Many materials such as carbon materials,[5,9–12] conductive polymers,[13,14] inorganic materials including metal nitrides,[15–17] carbides,[18,19] sulfides[20–23] and selenide,[24,25] and composites have been employed to replace Pt as the CE in DSSCs.

Among these counter electrode materials, transition metal carbides, such as molybdenum, tungsten, niobium and vanadium,[18,19] have been shown to have good catalytic activity for the reduction of triiodide to iodide in DSSCs. However, these metal carbides contain rare earth elements. Iron carbide (Fe_3C) seems more attractive for its abundance in the earth's crust and its high electronic conduction, higher resistance against oxidation and good catalytic activity[26] as well. However, iron carbide (Fe_3C) has been less investigated in DSSCs mainly because of the preconception that iron carbide is a metastable compound, which readily decomposes into α-Fe and carbon.[27] Moreover, α-Fe is susceptible to corrosion by I^-/I_3^- redox species.[28] Very recently, Fu *et al.* found that the Fe_3C could survive very well in a I^-/I_3^- electrolyte and a fair efficiency of 6.04% was obtained. However, as mentioned in this work, α-Fe coexisted in the compound and an additional etching process is required to remove the unstable α-Fe.[29]

For the counter electrode of DSSCs, electronic conductivity is as important as the catalytic activity to decrease the overvoltage and to thereby minimize energy losses.[30] It is known that the catalytic and electronic properties of transition metal compounds are governed by their intrinsic materials. However, bulk materials usually exhibit limited catalytic activity probably because of their large particle size and less specific surface area.[31] Nanostructure materials have been known to show better properties compared to their corresponding bulk materials. Therefore, it is of great significance to further explore highly

[a]The Qingdao Key Lab of solar energy utilization and energy storage technology, Qingdao Institute of Bioenergy and Bioprocess Technology, Chinese Academy of Sciences, Qingdao, 266101, P. R. China. E-mail: cuigl@qibebt.ac.cn; Fax: +8653280662744; Tel: +8653280662746

[b]University of Chinese Academy of Sciences, Beijing, 100049, P. R. China

[c]Qingdao University of Science and Technology, Qingdao, 266101, P. R. China

† Electronic supplementary information (ESI) available: XRD patterns of Fe_3C@N–C nanocomposites with different FeC_2O_4/NH_2CN ratios; Element analysis results of Fe_3C@N–C with different *R* values; SEM and TEM images of FeC_2O_4; TEM images of Fe_3C@N–C-1 and Fe_3C@N–C-4; Elemental mapping of Fe_3C@N–C nanocomposites; Raman spectra of Fe_3C@N–C-1, Fe_3C@N–C-2.5; Consecutive 100 cyclic voltammograms for the Fe_3C@N–C-2.5 CE; Equivalent circuits for the symmetric cells consisting of platinum and Fe_3C@N–C electrodes; SEM images of nearly pure N–C and non-1D configuration Fe_3C@N–C-2.5; Characteristics of the *J–V* curves of the DSSCs fabricated using nearly pure N–C and non-1D configuration Fe_3C@N–C-2.5. See DOI: 10.1039/c3ta14429a

‡ These authors contributed equally to this work.

efficient counter electrodes of transition metal compounds by the rational design of nanostructured catalytic materials. Among different kinds of nanoscale morphologies, one-dimensional nanostructures are known to be beneficial for electronic conduction along the axial direction.[22] Herein, iron carbide encaged in nitrogen-doped carbon (Fe_3C@N–C) nanowires were synthesized by directly annealing of iron(II) oxalate (FeC_2O_4) nanowires in H_2 atmosphere with cyanamide (NH_2CN) as the structure confinement agent. At the optimized annealing temperature, the composites with varied Fe_3C concentrations were explored as the counter electrode in DSSCs. Because of the synergetic effect of N–C and Fe_3C, and the presence of the one dimensional morphology, Fe_3C@N–C-2.5 (ratio of FeC_2O_4/CH_2N_2 is 2.5) nanostructures as counter electrodes exhibited comparable photovoltaic performances to those of Pt–FTO.

Experimental

Materials

Cetyltrimethylammonium bromide (CTAB), iron(II) chloride tetrahydrate ($FeCl_2 \cdot 4H_2O$), and andoxalic acid ($H_2C_2O_4$) were purchased from Sinopharm Chemical Reagent Co., Ltd., China. Iodine and 4-*tert*-butylpyridine were purchased form TCI. N719 dye ($Ru(dcbpy)_2(NCS)_2$, (dcbpy = 2,2-bipyridyl-4,4-dicarboxylato)) was purchased from Solaronix SA. TiO_2 paste and 1,2-dimethyl-3-propylimidazolium iodide were purchased from Wuhan GeAo Tech Co., Ltd., China. Guanidinium thiocyanate was purchased from Dalian HeptaChroma Solar Tech Co., Ltd., China. All the chemicals are analytical grade and were used without further purification.

Synthesis of Fe_3C@N–C

FeC_2O_4 nanowires were firstly synthesized as precursors of the Fe_3C product *via* a microemulsion route. 10 g CTAB which served as a soft template was added to a mixture of cyclohexane (300 mL) and *n*-pentanol (10 mL). After stirring for 30 min, 15 mL of 1 M $H_2C_2O_4$ and 5 mL of 1 M $FeCl_2 \cdot 4H_2O$ aqueous solution were added to the above microemulsion and stirred for another 24 h at ambient temperature. The yellow precipitate was filtered and washed with ethanol to remove impurities.[32] After being dried overnight in a vacuum oven at 50 °C, the as-synthesized FeC_2O_4 nanowires were dispersed in ethanol which contained a certain amount of NH_2CN for homogenous precursor mixing before heat treatment. After being dried again, the mixed raw powders were annealed at various temperatures for 2 h under a hydrogen atmosphere and the black Fe_3C@N–C nanocomposites were finally obtained. The obtained Fe_3C@N–C nanocomposites with weight ratios of FeC_2O_4/NH_2CN of 1, 2.5, 4 were labeled as Fe_3C@N–C-1, Fe_3C@N–C-2.5, Fe_3C@N–C-4.

Preparation of the counter electrodes

The mirror-like Pt/FTO electrode was obtained by electrodepositing a platinum layer on the surface of a fluorine-doped tin oxide substrate. The thickness of Pt films is about 75 nm. The Fe_3C@N–C (30 mg) and polyvinylidene fluoride dissolved in *N*-methyl-2-pyrrolidinone (10%, wt%) were ground together to generate a homogenous paste. Subsequently, the counter electrode films were prepared on a pre-cleaned fluorine-doped tin oxide (FTO) substrate by the doctor blade technique followed by heat drying at 60 °C for 24 h.

Fabrication of the DSSCs

TiO_2 working photoanodes were prepared on the FTO substrate using TiO_2 pastes by the doctor blade technique and subsequently sintered at 500 °C for 30 min in air. The resultant TiO_2 photoanodes were soaked in an ethanol solution of N719 dye (3×10^{-4} M) for 24 h to obtain dye-sensitized TiO_2 electrodes. The dye-adsorbed TiO_2 photoanodes with an active area of 0.16 cm^2 were assembled with Fe_3C@N–C and platinum counter electrodes using laboratory tape as a spacer to fabricate the corresponding sandwich-type cells, respectively. The liquid electrolyte is composed of 0.6 M 1,2-dimethyl-3-propylimidazolium iodide (DMPII), 0.03 M iodine (I_2), 0.06 M lithium iodide (LiI), 0.5 M 4-*tert*-butylpyridine (TBP), and 0.1 M guanidinium thiocyanate with acetonitrile (ACN) as the solvent.

Characterization

The morphologies of Fe_3C@N–C were investigated using field emission scanning electron microscopy (FESEM, HITACHI S-4800), and high-resolution transmission electron microscopy (HRTEM, JEOL 2010F). X-ray diffraction (XRD) patterns were recorded with a Bruker-AXS Micro-diffractometer (D8 ADVANCE) using Cu Kα radiation ($\lambda = 1.5406$ Å) from 20 °C to 70 °C. Cyclic voltammetry (CV) was carried out in a three-electrode system in an acetonitrile solution of 0.1 M $LiClO_4$, 10 mM LiI, and 1 mM I_2. Platinum served as a counter electrode and the non-aqueous Ag/Ag^+ couple was applied as a reference electrode. The photocurrent–voltage characteristics of the DSSCs were measured with a Newport (USA) solar simulator (300 W Xe source) and a Keithley 2440 source meter. Electrochemical impedance spectroscopy (EIS) measurements were performed using a Zahner Zennium electrochemical workstation by applying an AC voltage of 10 mV amplitude in the frequency range between 100 kHz and 100 mHz at room temperature. Fitting of impedance spectra to the proposed equivalent circuit was performed by using the Z view software.

Results and discussion

Fig. 1 depicts the XRD patterns of Fe_3C samples (Fe_3C@N–C-2.5) synthesized at 600 °C and 750 °C when the weight ratio of FeC_2O_4/NH_2CN is 2.5 ($R = 2.5$). After being annealed at 600 °C, all the peaks of the sample could be indexed to orthorhombic Fe_3C (JCPDS no. 65-2412) without any impurity phase, as shown in Fig. 1(b). However, when the reaction temperature was raised to 750 °C, two peaks corresponding to α-Fe were detected, as shown in Fig. 1(a). This is consistent with the previously reported results that the decomposition of Fe_3C into α-Fe and carbon occurred at $T > 600$ °C.[27] No diffraction peaks of graphite were observed which implied that the carbon component in the composites was amorphous due to the low annealing

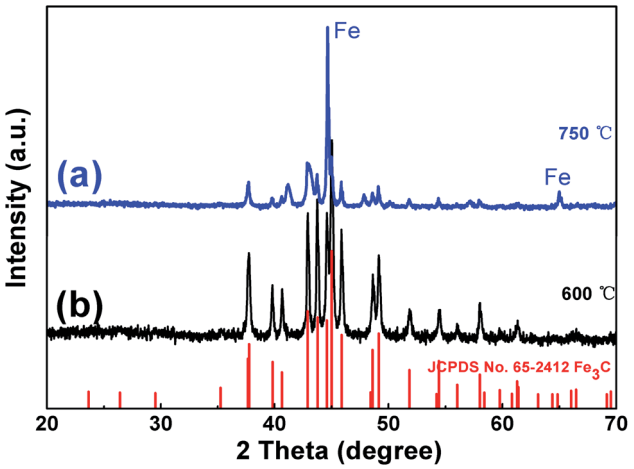

Fig. 1 Typical XRD patterns of Fe_3C samples synthesized at 750 °C and 600 °C.

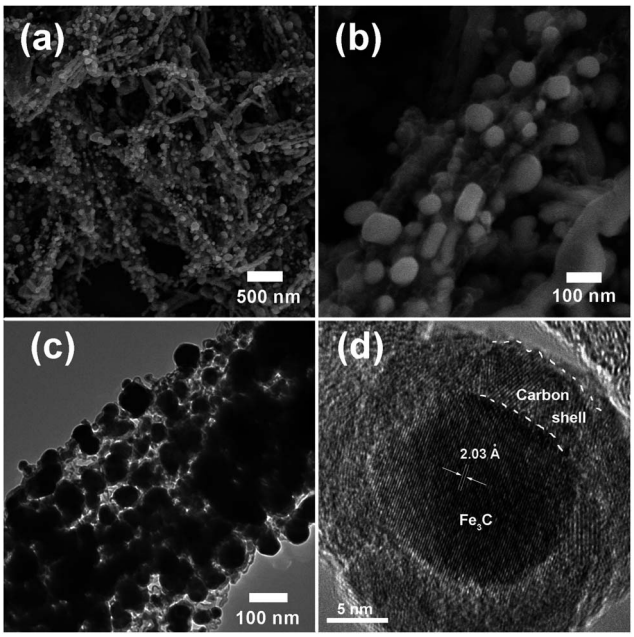

Fig. 2 Typical SEM and its enlarged images (a and b), TEM (c) and HRTEM (d) images of Fe_3C@N–C-2.5.

temperature. In order to avoid the generation of α-Fe which suffers from chemical instability in I^-/I_3^- electrolyte, the optimized reaction temperature was 600 °C. The influence of FeC_2O_4/NH_2CN ratio on product composition was also evaluated at the optimized temperature. As shown in Fig. S1,† both the patterns (for $R = 1$ and $R = 4.5$) exhibited the Fe_3C phase which coincides with the sample obtained at $R = 2.5$ (Fig. 1(b)). This implied that the FeC_2O_4/NH_2CN ratio may only change the relative amount of Fe_3C and carbon but does not affect the crystal structure of Fe_3C in final product. The elemental analysis results shown in Table S1† indicated the as-synthesized Fe_3C sample is comprised of C, N, Fe. It is reported that NH_2CN was condensed to C_3N_4 and decomposed into N-doped carbon (C–N) at high temperatures.[33] Therefore, the Fe_3C sample was the composite of Fe_3C and a minor amount of N-doped carbon. Meanwhile, the elemental analysis results indicated that with an increasing FeC_2O_4/NH_2CN ratio, the content of Fe_3C increased correspondingly in the as-prepared product.

Typical SEM and TEM images of as-synthesized FeC_2O_4 are shown in Fig. S2.† It can be clearly seen that the obtained FeC_2O_4 exhibits a one dimensional nanowire morphology and relatively smooth surface. After reaction with NH_2CN ($R = 2.5$), chain-like Fe_3C@N–C nanomaterials were observed as shown in Fig. 2(a) and most of the composites maintained the one dimensional morphology. This may be due to the appropriate amount of NH_2CN ($R = 2.5$) being added which could prevent nanowires from aggregation. When the FeC_2O_4/NH_2CN ratio was varied to 1 as shown in Fig. S3(a) and (b),† most of the Fe_3C nanowires displayed a rod-like aggregation structure which may be unfavorable to electronic transportation. When the FeC_2O_4/NH_2CN ratio was raised to 4, Fe_3C with minor carbon coatings were observed which are shown in Fig. S3(c) and (d),† where a good electronic connection would be difficult to achieve between isolated Fe_3C nanoparticles. However, from the enlarged micrographs shown in Fig. 2(b) and (c), Fe_3C nanoparticles with a size below 100 nm were well connected by N-doped carbon at $R = 2.5$. This unique structure is expected to be beneficial to the electron transfer during the catalytic reaction. The HRTEM shown in Fig. 2(d) confirmed that the Fe_3C nanoparticles were well encapsulated by a N-doped carbon layer with a fringe spacing of 2.03 Å corresponding to the (112) planes of orthorhombic Fe_3C.[34] In addition, elemental mapping in Fig. S4† elucidated that Fe, C and N were homogenously distributed in the composites. The much narrower D and G peak width in Fig. S5† implies that the carbon of Fe_3C@N–C-2.5 was more crystalline than that of Fe_3C@N–C-1. From the above results, well-wired Fe_3C nanoparticles, as well as the carbon sheath in the Fe_3C@N–C nanocomposite may mean this material is expected to present wonderful catalytic activity when used as the CE in DSSCs.

Cyclic voltammetry (CV) was performed to evaluate the electrocatalytic activity of the counter electrodes to reduce triiodide using a three-electrode system. CV curves for the I_3^-/I^- redox reaction obtained on Fe_3C@N–C and the reference Pt counter electrodes at a scan rate of 20 mV s^{-1} are shown in Fig. 3. Counter electrodes with good electrocatalytic activity for I_3^-/I^- electrolyte display two typical pairs of redox peaks, A_{ox}/A_{red} and B_{ox}/B_{red}. The A_{ox}/A_{red} is assigned to the redox reaction shown in eqn (1) and B_{ox}/B_{red} is ascribed to redox reaction shown in eqn (2).[35] From Fig. 3, it can be seen the CV curves of the CEs with Fe_3C@N–C displayed two pairs of redox peaks, indicating that they all possess electrocatalytic ability for the reduction of triiodide ions. A higher reduction peak current density (J_{red}) and a lower peak-to-peak voltage separation (E_{PP}) indicate a better catalytic activity. The redox peaks (A_{ox} and A_{red}) directly affects the DSSC performance. Therefore, we focused on the investigation of the peak current density (J_{red}) and peak-to-peak voltage separation (E_{PP}) of A_{ox} and A_{red}. The profile and location of the A_{ox} and A_{red} redox peaks of Fe_3C@N–C CEs were close to those of the Pt CE. This indicated the Fe_3C@N–C CEs

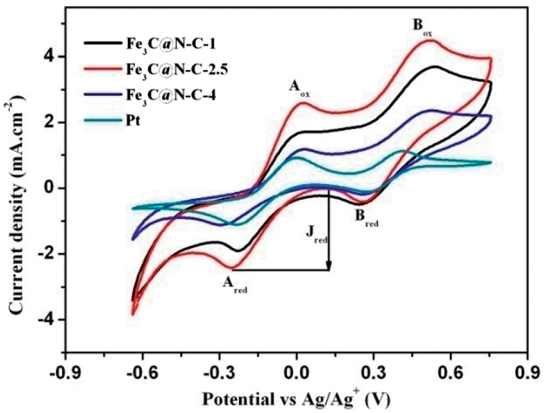

Fig. 3 Cyclic voltammograms of Pt and Fe_3C@N–C counter electrodes with different raw materials ratio in 10 mM LiI, 1 mM I_2 and 0.1 M $LiClO_4$ acetonitrile solution at a scan rate of 20 mV s^{-1}.

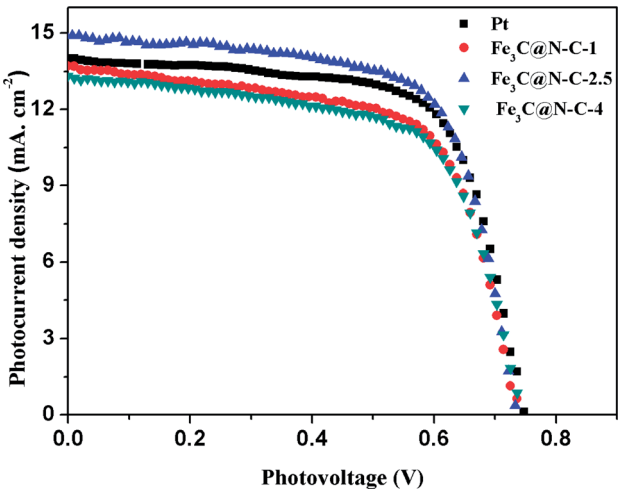

Fig. 4 Characteristic photocurrent density–voltage (*J–V*) curves of DSSCs with different electrodes, measured under simulated sunlight 100 mW cm^{-2} (AM 1.5). The liquid electrolyte is composed of 0.6 M 1,2-dimethyl-3-propylimidazolium iodide (DMPII), 0.03 M iodine (I_2), 0.06 M lithium iodide (LiI), 0.5 M 4-*tert*-butylpyridine (TBP), and 0.1 M guanidinium thiocyannate in acetonitrile solution.

and Pt CE possessed similar E_{pp} values. However, the cathodic current density increased in the order of Fe_3C@N–C-4 (1.15 mA cm^{-2}) < Pt (1.21 mA cm^{-2}) < Fe_3C@N–C-1 (1.68 mA cm^{-2}) < Fe_3C@N–C-2.5 (2.41 mA cm^{-2}). By comprehensive consideration of the E_{pp} and peak current density, the Fe_3C@N–C-2.5 presented slightly closer E_{pp} but much larger cathodic current density than that of the Pt CE, demonstrating a relatively better electrocatalytic activity than that of the Pt CE. The enhanced electrocatalytic activity can be attributed to the synergistic effect of the combination of high catalytic activity and good electrical conductivity of nitrogen-doped carbon into Fe_3C, and the nanowire morphology which is beneficial to electron transfer.[36] Fig. S6† shows 100-cycle CVs for the Fe_3C@N–C-2.5 electrode at a scan rate of 20 mV s^{-1}. They present an almost unchanged curves shape and constant redox peak current densities, indicating a comparable electrochemical stability of the Fe_3C@N–C-2.5 CE.

$$I_3^- + 2e^- \rightleftharpoons 3I^- \quad (1)$$

$$3I_2 + 2e^- \rightleftharpoons 2I_3^- \quad (2)$$

The photocurrent density–voltage (*J–V*) characteristic curves of the DSSCs fabricated with different counter electrodes measured under the illumination of 1 sun (100 mW cm^{-2}) are shown in Fig. 4. The photovoltaic parameters of these devices, including the short-circuit current (J_{sc}), the open-circuit voltage (V_{oc}), the fill factor (FF), and the energy conversion efficiency (η), are summarized in Table 1. All devices with the CEs containing Fe_3C had similar V_{oc}. However, the J_{sc} and FF complied with the order Fe_3C@N–C-2.5 > Pt > Fe_3C@N–C-1 > Fe_3C@N–C-4. This is in accordance with the results of CVs measurements. The DSSCs with Fe_3C@N–C counter electrodes exhibited a relatively higher η. The Fe_3C@N–C-1, Fe_3C@N–C-2.5, and Fe_3C@N–C-4 give η of 6.52%, 7.36%, and 6.36%, respectively. The DSSCs with a Fe_3C@N–C-2.5 CE possessed the best energy conversion efficiencies of 7.36% which was comparable to that of the DSSCs with a Pt CE (7.15%).

In order to further evaluate the electrochemical activity of the composite materials as counter electrodes in DSSCs, the electrochemical impedance spectra (EIS) were measured in a symmetric sandwich cell configuration consisting of two identical counter electrodes. Their Nyquist plots are illustrated in Fig. 5. For comparison, the impedance spectrum of the cell consisting of the conventional platinized electrodes was also presented here.

For a conventional symmetric cell consisting of platinized electrodes, the electric circuit elements should have a series resistance (R_s), a constant phase element (CPE), the charge transfer resistance (R_{ct}) and Nernst diffusion impedance of the I_3^-/I^- redox species within a thin layer in the electrolyte.[37] However, for a symmetric cell based on Fe_3C@N–C electrodes, three semicircles were visible for Fe_3C@N–C compared with two semicircle of the conventional Pt. The semicircle in the high frequency region was speculated to correspond to impedance arising from the Fe_3C@N–C–FTO interface ($R_{ct}(S)$).[38] The one in the middle frequency region is associated with the charge-transfer resistance of the counter electrode–redox (I^-/I_3^-) interface and the capacitance of the counter electrode–electrolyte interface. The low-frequency semicircle is attributed to Nernst diffusion impedance of the I_3^-/I^- redox species within a thin layer in the electrolyte. The intercept of the real axis at high frequency represents the ohmic series resistance including the sheet resistance of two identical CEs and the electrolytic resistance. The equivalent circuit is given in the Fig. S7† and the simulated data from the EIS spectra for Fe_3C@N–C and Pt are summarized in Table 2. The Fe_3C@N–C CEs had slightly larger R_s values than the Pt CE (Table 2), indicating that Fe_3C@N–C had relatively lower conductivity compared to Pt. The impedance arising from the Fe_3C@N–C–FTO interface of Fe_3C@N–C-1, Fe_3C@N–C-2.5 and Fe_3C@N–C-4 are 7.10 Ω, 5.58 Ω, and 2.83 Ω. The results demonstrated that bonding strength

Table 1 Characteristics of the *J*–*V* curves of the DSSCs fabricated using different counter electrodes[a]

Counter electrode	J_{sc} (mA cm^{-2})	V_{oc} (mV)	FF (%)	η (%)
Fe_3C@N–C-1	13.74	738	64.31	6.52 ± 0.04
Fe_3C@N–C-2.5	14.97	741	66.35	7.36 ± 0.03
Fe_3C@N–C-4	13.39	741	64.08	6.36 ± 0.04
Pt	14.13	747	67.71	7.15 ± 0.02

[a] V_{oc}: open circuit voltage, J_{sc}: short circuit current density, FF: fill factor, η: energy conversion efficiency.

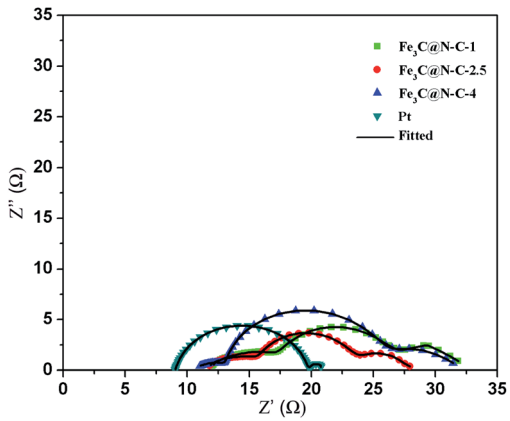

Fig. 5 Nyquist plots for the symmetric cells fabricated with two identical counter electrodes of Fe_3C@ N–C-1 (■), Fe_3C@ N–C-2.5 (●), Fe_3C@ N–C-4 (▲), Pt (▼). The lines express fit results for the corresponding EIS data. The cells were measured within the frequency range between 100 kHz and 100 mHz.

between Fe_3C@N–C and FTO became stronger with the increase of the content of Fe_3C. The simulated charge-transfer resistances of Fe_3C@N–C-1, Fe_3C@N–C-2.5, and Fe_3C@N–C-4 counter electrodes are 7.77 Ω, 6.78 Ω, and 12.3 Ω respectively. The charge-transfer resistances Fe_3C@N–C-1 and Fe_3C@N–C-2.5 are much lower than that of the Pt electrode (10.65 Ω), suggesting the higher electrocatalytic activity of Fe_3C@N–C electrodes over the Pt-FTO electrode for the reduction of triiodide ions. The charge-transfer resistance of Fe_3C@N–C-2.5 is much lower than that of other Fe_3C@N–C electrodes which may be attributed to efficient electrocatalytic activity from the optimal interaction between the Fe_3C and carbon, and the enhanced electron transport capability contributed by the nanowire morphology.[36] The enhanced charge-transfer resistance of Fe_3C@N–C-4 may be due to the decreased content of carbon which decreased the electrocatalytic activity of the Fe_3C@N–C composites. The EIS results agree with the CV data. The lower resistance would endow a greater FF and higher η in the solar cell which is corroborated by the corresponding performance measurement.

Table 2 EIS parameters of the symmetric cells based on different counter electrodes[a]

Counter electrode	R_s (Ω)	R_{ct} (Ω)	$R_{ct}(S)$ (Ω)
Fe_3C@N–C-1	10.9	7.77	7.10
Fe_3C@N–C-2.5	10.75	6.78	5.58
Fe_3C@N–C-4	10.38	12.3	2.83
Pt	9.04	10.65	~

[a] R_s: series resistance, R_{ct}: charge-transfer resistance, $R_{ct}(S)$: impedance arising from the Fe_3C@N–C–FTO interface.

Conclusions

In summary, a N–C and Fe_3C nanocomposite (Fe_3C@N–C) was fabricated by carbothermal reduction using cyanamide as the nitrogen and carbon source. An appropriate amount of NH_2CN prevented the aggregation of the FeC_2O_4 nanowires and generated a favorable carbon-coating at 600 °C. Dye-sensitized solar cells with Fe_3C@N–C nanocomposite films as the counter electrodes were explored. Among these DSSCs fabricated from Fe_3C@N–C, Fe_3C@N–C-2.5 yielded the highest photoelectrical conversion efficiency of 7.36%. That is because of the synergetic combination of the N-doped carbon and Fe_3C, generating better catalytic performance and lowest charge-transfer resistance. Moreover, the Fe_3C@N–C-2.5 nanowire configuration is favorable for fast electron transfer. The abundance of the Fe element and the facile synthesis method make Fe_3C-based nanocomposites promising candidates for large-scale, highly efficient and low-cost counter electrodes for DSSCs.

Acknowledgements

This work was supported by National Program on Key Basic Research Project of China (973 Program) (no. MOST2011CB935700), the National Natural Science Foundation (Grant no. 21202178, 21271180), the Shandong Province Natural Science Foundation (Grant no. ZR2011BQ024, ZR2013FZ001 and ZR2010BM016).

Notes and references

1 B. O'Regan and M. Grätzel, *Nature*, 1991, **353**, 737–740.
2 M. Grätzel, *Nature*, 2001, **414**, 338–344.
3 L. M. Peter, *Phys. Chem. Chem. Phys.*, 2007, **9**, 2630–2642.
4 N. Yang, J. Zhai, D. Wang, Y. Chen and L. Jiang, *ACS Nano*, 2010, **4**, 887–894.
5 X. Wang, L. Zhi and K. Müellen, *Nano Lett.*, 2007, **8**, 323–327.
6 J. Wang and Z. Lin, *Chem. – Asian J.*, 2012, **7**, 2754–2762.
7 N. Papageorgiou, *Coord. Chem. Rev.*, 2004, **248**, 1421–1446.
8 E. Olsen, G. Hagen and S. Eric Lindquist, *Sol. Energy Mater. Sol. Cells*, 2000, **63**, 267–273.
9 H. Wang, K. Sun, F. Tao, D. J. Stacchiola and Y. H. Hu, *Angew. Chem., Int. Ed.*, 2013, **52**, 9210–9214.
10 M. Wu, X. Lin, T. Wang, J. Qiu and T. Ma, *Energy Environ. Sci.*, 2011, **4**, 2308–2315.
11 Z. Yang, M. Liu, C. Zhang, W. W. Tjiu, T. Liu and H. Peng, *Angew. Chem., Int. Ed.*, 2013, **52**, 3996–3999.
12 H. Wang and Y. H. Hu, *Energy Environ. Sci.*, 2012, **5**, 8182–8188.

13 H. Wang, Q. Feng, F. Gong, Y. Li, G. Zhou and Z.-S. Wang, *J. Mater. Chem. A*, 2013, **1**, 97–104.
14 (*a*) Q. Tai, B. Chen, F. Guo, S. Xu, H. Hu, B. Sebo and X.-Z. Zhao, *ACS Nano*, 2011, **5**, 3795–3799; (*b*) T.-L. Zhang, H.-Y. Chen, C.-Y. Su and D.-B. Kuang, *J. Mater. Chem. A*, 2013, **1**, 1724–1730.
15 Q. W. Jiang, G. R. Li and X. P. Gao, *Chem. Commun.*, 2009, 6720–6722.
16 M. Wu, Q. Zhang, J. Xiao, C. Ma, X. Lin, C. Miao, Y. He, Y. Gao, A. Hagfeldt and T. Ma, *J. Mater. Chem.*, 2011, **21**, 10761–10766.
17 X. Zhang, X. Chen, S. Dong, Z. Liu, X. Zhou, J. Yao, S. Pang, H. Xu, Z. Zhang, L. Li and G. Cui, *J. Mater. Chem.*, 2012, **22**, 6067–6071.
18 M. Wu, X. Lin, A. Hagfeldt and T. Ma, *Angew. Chem., Int. Ed.*, 2011, **50**, 3520–3524.
19 M. Wu, X. Lin, Y. Wang, L. Wang, W. Guo, D. Qi, X. Peng, A. Hagfeldt, M. Grätzel and T. Ma, *J. Am. Chem. Soc.*, 2012, **134**, 3419–3428.
20 M. Wang, A. M. Anghel, B. Marsan, N.-L. Cevey Ha, N. Pootrakulchote, S. M. Zakeeruddin and M. Grätzel, *J. Am. Chem. Soc.*, 2009, **131**, 15976–15977.
21 Z. Ku, X. Li, G. Liu, H. Wang, Y. Rong, M. Xu, L. Liu, M. Hu, Y. Yang and H. Han, *J. Mater. Chem. A*, 2013, **1**, 237–240.
22 C.-W. Kung, H.-W. Chen, C.-Y. Lin, K.-C. Huang, R. Vittal and K.-C. Ho, *ACS Nano*, 2012, **6**, 7016–7025.
23 X. Xin, M. He, W. Han, J. Jung and Z. Lin, *Angew. Chem., Int. Ed.*, 2011, **50**, 11739–11742.
24 F. Gong, H. Wang, X. Xu, G. Zhou and Z.-S. Wang, *J. Am. Chem. Soc.*, 2012, **134**, 10953–10958.
25 (*a*) Z. Zhang, S. Pang, H. Xu, Z. Yang, X. Zhang, Z. Liu, Z. Wang, X. Zhou, S. Dong, X. Chen, L. Gu and G. Cui, *RSC Adv.*, 2013, **3**, 16528–16533; (*b*) F. Gong, X. Xu, Z. Li, G. Zhou and Z.-S. Wang, *Chem. Commun.*, 2013, **49**, 1437–1439.
26 Z. Wen, S. Ci, F. Zhang, X. Feng, S. Cui, S. Mao, S. Luo, Z. He and J. Chen, *Adv. Mater.*, 2012, **24**, 1399–1404.
27 C. Giordano, A. Kraupner, I. Fleischer, C. Henrich, G. Klingelhofer and M. Antonietti, *J. Mater. Chem.*, 2011, **21**, 16963–16967.
28 J. C. Wren, G. A. Glowa and J. Merritt, *J. Nucl. Mater.*, 1999, **265**, 161–177.
29 Y. Liao, K. Pan, L. Wang, Q. Pan, W. Zhou, X. Miao, B. Jiang, C. Tian, G. Tian, G. Wang and H. Fu, *ACS Appl. Mater. Interfaces*, 2013, **5**, 3663–3670.
30 J. Halme, M. Toivola, A. Tolvanen and P. Lund, *Sol. Energy Mater. Sol. Cells*, 2006, **90**, 872–886.
31 J. Qi, L. Jiang, Q. Jiang, S. Wang and G. Sun, *J. Phys. Chem. C*, 2010, **114**, 18159–18166.
32 N. Du, Y. Xu, H. Zhang, C. Zhai and D. Yang, *Nanoscale Res. Lett.*, 2010, **5**, 1295–1300.
33 Y.-S. Jun, W. H. Hong, M. Antonietti and A. Thomas, *Adv. Mater.*, 2009, **21**, 4270–4274.
34 Q. Su, J. Li, G. Du and B. Xu, *J. Phys. Chem. C*, 2012, **116**, 23175–23179.
35 A. I. Popov and D. H. Geske, *J. Am. Chem. Soc.*, 1958, **80**, 1340–1352.
36 (*a*) J. Song, G. R. Li, F. Y. Xiong and X. P. Gao, *J. Mater. Chem.*, 2012, **22**, 20580–20585; (*b*) G.-R. Li, F. Wang, Q.-W. Jiang, X.-P. Gao and P.-W. Shen, *Angew. Chem., Int. Ed.*, 2010, **49**, 3653–3656.
37 F. Fabregat-Santiago, J. Bisquert, E. Palomares, L. Otero, D. Kuang, S. M. Zakeeruddin and M. Grätzel, *J. Phys. Chem. C*, 2007, **111**, 6550–6560.
38 (*a*) T. N. Murakami, S. Ito, Q. Wang, M. K. Nazeeruddin, T. Bessho, I. Cesar, P. Liska, R. Humphry-Baker, P. Comte, P. t. Péchy and M. Grätzel, *J. Electrochem. Soc.*, 2006, **153**, A2255–A2261; (*b*) P. Joshi, Z. Zhou, P. Poudel, A. Thapa, X.-F. Wu and Q. Qiao, *Nanoscale*, 2012, **4**, 5659–5664.